Molecular dynamics simulations of high-energy radiation damage in W and W−Re alloys

Jun Fu [a], Yangchun Chen [a], Jingzhong Fang [a], Ning Gao [b, c, **], Wangyu Hu [a], Chao Jiang [a], Hong-Bo Zhou [d], Guang-Hong Lu [d], Fei Gao [e], Huiqiu Deng [a, *]

[a] *School of Physics and Electronics, College of Materials Science and Engineering, College of Mechanical and Vehicle Engineering, Hunan University, Changsha, 410082, China*
[b] *Institute of Modern Physics, Chinese Academy of Sciences, Lanzhou, 730000, China*
[c] *School of Nuclear Science and Technology, Chinese Academy of Sciences, Beijing, 100094, China*
[d] *Department of Physics, Beihang University, Beijing, 100191, China*
[e] *Department of Nuclear Engineering and Radiological Science, University of Michigan, Michigan, 48109, USA*

HIGHLIGHTS

- Formation of completed 1/2<111> and mixed 1/2<111>−<100> interstitial loops during high-energy neutron cascades in W and W−Re alloys.
- High-energy cascade induces a unique loop configuration taking the same Burgers vector but locating on different habit planes.
- Re does not significantly affect the number of surviving defects.
- Re reduces the mobility of the interstitial clusters and loops.

ARTICLE INFO

ABSTRACT

High-energy collision cascades with an energy of up to 300 keV for the primary knock-on atom (PKA) have been initially simulated in W and W−Re alloys containing 5 or 10 at.% Re atoms using the molecular dynamics method with recently fitted W−Re interatomic potentials. The effects of PKA energy and Re concentration on defect production, defect clustering and states of dislocation loops have been quantitatively analysed. The results show that the presence of Re atoms does not significantly affect either the number of surviving defects or their clustered fractions. In addition, the interstitial dislocation loops are dominated by the 1/2<111> loops. Mixed interstitial loops with 1/2<111> and <100> Burgers vectors and interstitial loops that have the same Burgers vectors but are located on different habit planes have also been observed. Further analysis indicates that the pinning effect induced by the Re atom segregation leads to the lower mobility of the interstitial clusters and interstitial 1/2<111> loops in W−Re alloys than in pure W, which is expected to influence the subsequent evolution of radiation-induced defects in W−Re alloy.

1. Introduction

Tungsten (W) and W-based alloys have received particular attention as possible candidates for plasma-facing materials (PFMs) in future fusion reactors because of their high melting point, excellent thermal conductivity and good sputtering resistance [1−4]. However, some transmutation elements, such as rhenium (Re), osmium (Os), tantalum (Ta) and hafnium (Hf), will be produced through nuclear transmutation reactions in W induced by high-energy neutrons in fusion reactors [5,6]. Furthermore, these transmutation elements, particularly Re, have been confirmed to critically affect the performance of PFMs during and after irradiation. For example, various experimental studies have demonstrated that neutron irradiation can cause the gathering and precipitation of Re atoms, resulting in the formation of σ-phase (WRe) or χ-phase

* Corresponding author. School of Physics and Electronics, Hunan University, Changsha, 410082, China.
** Corresponding author. School of Nuclear Science and Technology, Chinese Academy of Sciences, Beijing, 100094, China.
E-mail addresses: ning.gao@impcas.ac.cn (N. Gao), hqdeng@hnu.edu.cn (H. Deng).

(WRe$_3$) in W−Re alloys [7−11] despite the Re concentration is considerably lower than its dissolution limit (approximately 26 at.%). These precipitates will lead to radiation hardening and embrittlement of the W materials and critically affect the lifetime of these PFMs used in future fusion reactors [10−14]. Therefore, understanding the Re effect at the primary state of damage because of the displacement cascades is a key and necessary step to model the neutron irradiation damages in W and W-based alloys.

In addition to the formation of W−Re precipitates, high-energy neutrons produced by the deuterium−tritium fusion plasma can induce primary recoils with primary knock-on atom (PKA) energy up to hundreds of keV. For example, direct knock-on elastic collisions with 14.1-MeV fusion neutrons will result in W recoils having a maximum kinetic energy of $E_{max} = 4\frac{mM}{(m+M)^2}E_n$ ~300 keV (m and M denote the mass of the neutron and W atom, respectively), which will produce critical displacement damages such as Frenkel pairs (FPs), vacancies, interstitials, vacancy/interstitial clusters and voids as well as dislocation loops. These collisions are also expected to interact with the Re atoms in W−Re alloy, affecting the properties of these materials. Therefore, understanding the cascade evolution after the appearance of Re atoms in W is necessary, particularly with PKA energy (E_{PKA}) up to 300 keV.

In previous studies, majority of the cascades obtained through molecular dynamics (MD) simulations in case of pure W have focused on the radiation damages caused when E_{PKA} is less than 100 keV [15−23], and only few studies have been conducted with high PKA energies of up to 300 keV. Sand et al. [24,25] conducted a study with E_{PKA} of up to 150 keV in pure W. This result denoted that the size distribution of the defect clusters followed a power law function, $f(n) = A/n^S$. Here, n, A and S denote the size of a defect cluster, the pre-factor proportional to the experimental or simulated defect cluster production rate and the scaling exponent, respectively. Zarkadoula et al. [26] conducted another study with high E_{PKA} of up to 300 keV. The result indicated that a limited fraction of damages was produced via electron−phonon coupling after the electronic effects. However, until now, no detailed study has investigated the effects of the Re atoms on the initial stage of displacement cascades in W−Re alloys with E_{PKA} of up to 300 keV. As stated above, it is necessary and important to explore the physics of this stage to understand the radiation damages related with the appearance of Re atoms in W. Thus, in this study, on the basis of the recently developed Finnis−Sinclair (F−S) W−Re interatomic potential by our group [27], the displacement cascades with PKA energies ranging from 1 to 40 keV have been initially simulated and then compared with the results obtained from previous studies using pure W. The high-energy collision cascades in pure W, W−5-at.% Re and W−10-at.% Re alloys, with PKA energies of up to 300 keV, are simulated. As the main step in understanding the effect of Re on the radiation damages in alloys, the solid solution W−Re alloys containing W atoms that are randomly replaced by Re atoms to a given concentration are selected as the matrix for performing cascade simulations. Hence, the effects induced by the presence of Re at high-energy cascade stages in W bulks can be explored. In this study, we mainly focus on the effect of the transmutation element Re on the radiation damages in the W bulk materials. Further, the electronic effects have not yet been considered. The electron−phonon coupling is not considered, and electronic stopping during the evaluation of interatomic forces is also not included during simulations. Such electronic effects could be investigated in the future after the parameters used in the two temperature models [28,29] have been quantitatively determined. The remainder of this study is organised as follows. The simulation methods are introduced in Section 2, and the results and discussion based on the MD simulations are provided in Section 3. Finally, the conclusions of this study are presented in Section 4.

2. Simulation methods

All the MD simulations in this study are performed using the LAMMPS code [30]. The W−W, Re−Re and W−Re interactions are determined using the recently developed F−S type interatomic potentials [27], which were fitted with emphasis on the formation and binding energies of various radiation defects in bulk W and W−Re alloys. The W potential accurately predicts that a 1/2<111> dislocation loop has lower formation energy than that of a <100> loop containing the same number of self-interstitial atoms in W at low temperatures. To appropriately simulate the collision cascades, especially for accurate description of interaction induced by two atoms at a short distance ($r < r_m$), the pair interaction functions (V_{WW}, V_{ReRe}, and V_{WRe}) obtained from Ref. [27] are combined with the Ziegler−Biersack−Littmark (ZBL) universal function [31] through a connection function.

$$V(\text{r}) = e^{(b_0+b_1r+b_2r^2+b_3r^3)}(r_m \le r \le r_n),$$

where the parameters $b_0 - b_3$ are determined by fitting to the short and long-range potentials at cutting points r_m and r_n, respectively. These parameters for the ZBL universal function are presented in Table 1. The threshold displacement energy (E_d) is the minimum recoil energy required by a lattice atom to be permanently displaced to an interstitial position, forming stable FPs. In our simulations, E_d along the <100> direction calculated using our interatomic potential is 34 eV in case of W, which is slightly lower than the experimental value of 42 eV [32]. The predicted displacement threshold energies along the <100> direction calculated using the W potentials of Ackland and Thetford [33], Juslin and Wirth [34] and Marinica et al. [35] were 57, 63 and 31 eV, respectively, as reported by Sand et al. [36]. The predicted E_d values are observed to be clearly dependent on the used potentials. Further, Sand et al. [36] simulated defect production using various potentials and observed that the effect of potentials on defect numbers is not significant even although their predicted displacement threshold energies are different, as previously discussed. Subsequently, we calculated E_d for the other six directions and, on the basis of these calculations, determined the average E_d of our potential to be 92 eV, which is in good agreement with the value of 90 eV reported in an experimental study [37].

High-energy displacement cascades are simulated in body-centred cubic pure W, W−5 at.% Re and W−10 at.% Re alloys, where Re atoms are randomly distributed at the substitutional positions of the W matrix, forming solid solution W−Re alloys. Table 2 indicates that the size of the computational boxes is dependent on E_{PKA}, with the maximum number of atoms observed to be 16 million. Furthermore, periodic boundary conditions are used in all the three dimensions. A Nosé−Hoover [38] thermostat is applied on the outermost layer of the box with a thickness of approximately 3 lattice units to regulate the atomic velocities based on the target temperature. The total energy of the system is initially

Table 1
Parameters for the connection function.

	W	Re	WRe
b_0	10.6264260368211	11.6663350590345	10.1095270894606
b_1	−4.52597536152745	−5.57386927577885	−3.93159538928197
b_2	0.122451273514719	−0.105792452184853	0.253356338120054
b_3	−0.146815276239037	0.105513289561141	−0.347153104693508
r_m	1.0	1.0	1.0
r_n	2.0	2.0	2.0

Table 2
Parameters of PKA energies (E_{PKA}), simulation time, box length (in the unit of lattice constant $a_0 = 3.1652$ Å) and the number of events studied in pure W, W−5 at.% Re and W−10 at.% Re alloys.

E_{PKA} (keV)	Simulation time (ps)	Box length (a_0)	Number of events		
			W	W-5 at.% Re	W-10 at.% Re
1	50	40	20		
2	50	40	20		
5	50	40	20		
10	50	60	20		
20	50	60	20		
30	50	60	20		
40	50	80	20		
100	100	120	30	30	30
200	100	200	30	30	30
300	100	200	30	30	30

minimised using a conjugate gradient method. Further, the MD simulations are conducted at 300 K under zero pressure for 30 ps (ps) using an NPT ensemble with a time step of 1 fs (fs). After complete relaxation, a cascade is initiated by displacing a randomly selected PKA at the centre of the MD block with an initial velocity along the high-index direction <135> to avoid channelling effect [39]. During the displacement cascade process, simulations are performed under the microcanonical NVE ensemble for all the atoms; however, three lattice atomic layers at the boundaries are maintained under the NVT ensemble with the Nosé−Hoover [38] thermostat. The time step is automatically adapted between 10^{-3} and 10^{-7} ps, and the total time required for cascade simulation varies from 50 to 100 ps, depending on the E_{PKA}. Considering the differences between individual cascades, 20−30 cascades are repeated for each case with various PKA energies to obtain statistical results. The parameters of the PKA energies, simulation time, box length and number of events, with a total of more than 410 simulated cascades, are presented in Table 2.

The formed interstitials and vacancies are identified using the Wigner−Seitz (W−S) cell method [40], where an empty W−S cell without any W or Re atom is considered to be vacant and two or more W (or Re) atoms in the same W−S cell are considered to contain one or more interstitial atoms. On the basis of previously conducted studies [19,21,22,24,41], the distance of the second- or third-nearest neighbour is used as the cut-off radius to define the interstitial or vacancy cluster, respectively. Further, the sizes of the defect clusters involved in this study are determined based on the net defect count, which is the result of the difference between the number of interstitials and vacancies. In this study, we treat three or more vacancy agglomerations and four or more interstitial agglomerations as clusters. Finally, the formed dislocation loops during the cascading processes are analysed using the Open Visualization Tool (OVITO) [42] and the implemented dislocation extraction algorithm (DXA) [43].

3. Results and discussion

3.1. Defect production

Prior to investigating high-energy cascades, we primarily simulated the low-energy cascades in pure W with PKA energies ranging from 1 to 40 keV at 300 K. Further, we compared the average number of surviving FPs with that in the previous reports of Caturla et al. [16], Fikar et al. [18], Troev et al. [20] and Warrier et al. [23] using different interatomic potentials [33,44−46]. Table 3 presents the obtained simulation results. From the table, the number of surviving FPs (N_{FP}) obtained at low PKA energies with various interatomic potentials agrees very well with the present results. On the basis of the average number of surviving FPs from

Table 3
The average number of surviving Frenkel pairs (FPs) obtained from MD with PKA energies 1−40 keV in pure W. The comparisons with previous studies by Caturla et al. [16], Fikar et al. [18], Troev et al. [20] and Warrier et al. [23] using different interatomic potentials [33,44−46] are also provided. The values in brackets denote the standard errors of the mean.

E_{PKA} (keV)	Caturla [16]	Fikar [18]	Troev [20]	Warrier [23]	This work
1	4		4	3(1)	3(1)
2	6		7	5(2)	6(2)
5	8		8	10(3)	10(2)
10	9	10(1)	10		16(3)
20	18	18(1)	18		22(4)
30	37		33		32(5)
40			42		43(7)

different potentials, the defect production in W is likely to be correlated with the average E_d rather than along a specific direction. Therefore, the present potential [27] can be reasonably utilised for performing further cascade simulations.

High-energy collision cascades in pure W, W−5 at.% Re and W−10 at.% Re alloys have been simulated with PKA energies from 100 to 300 keV. Fig. 1 depicts the dependence of N_{FP} as a function of E_{PKA} (1−300 keV), denoting that N_{FP} increases with E_{PKA} in pure W. The dependence can be separated into two regions and described using the same function but with different values for parameters a
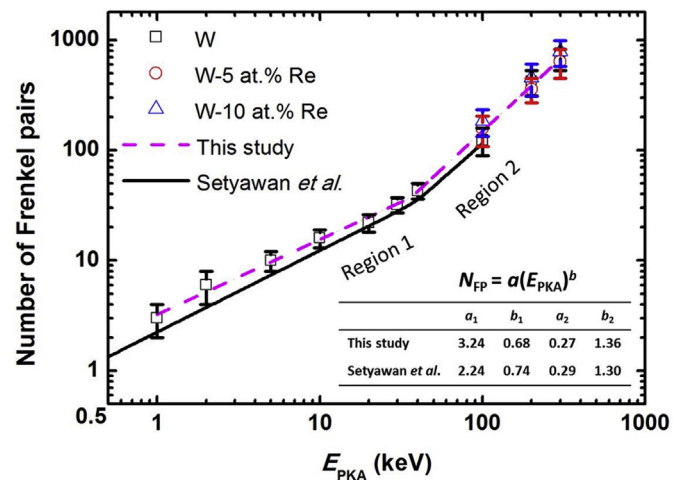

Fig. 1. (Color online) Dependence of the number of surviving FPs on the PKA energy, E_{PKA}; a comparison between results obtained at 300 K by Setyawan et al. (black solid line [22]) and the current findings is also included in the figure. The error bars denotes the average standard errors. (For interpretation of the references to color in this figure legend, the reader is referred to the Web version of this article.)

and b: $N_{FP} = a\,(E_{PKA})^b$. A similar relation has also been reported for defect production in W cascades with PKA energies ranging from 1 to 100 keV, as presented by Setyawan et al. [22]. Their results are also presented in Fig. 1 for comparison. The lower- and higher-energy regions are denoted as Region 1 and Region 2, respectively. In Region 1, the fitted exponent is 0.7 ± 0.04, which is close to the value presented in Ref. [22]. However, a slightly large pre-factor of 3.24 (2.24 from Ref. [22]) is obtained in this study. In the high-energy region, the pre-factor and exponent, both close to those mentioned in Ref. [22], are obtained. According to the analysis of Setyawan et al., the intersection of the two fitted lines is defined as the transition energy that marks the morphological transition of cascades and the beginning of the formation of large self-interstitial atom (SIA) clusters (size of 14 or more) [22,47]. In this study, such a transition occurs with E_{PKA} of approximately 38 keV, close to the prediction of 35 keV at 300 K according to the results of Setyawan et al. [22]. Presumably, the number of surviving FPs produced at 200 and 300 keV follows the same dependence on E_{PKA} in Region 2.

To confirm the correlation between the transition energy and the onset of large interstitial cluster formation, two figures are presented in Fig. 2, denoting the dependence of the SIA cluster size on the E_{PKA} of pure W, including the average size of the largest SIA clusters and the number of SIA clusters of size ≥ 14 (the SIA clusters comprising 14 interstitials or more generally form interstitial dislocation loops) per cascade. To calculate the average size of the largest SIA clusters per E_{PKA}, we considered only the largest SIA cluster from each simulated event and then averaged over the total number of events for the same E_{PKA}. Below the transition energy (Fig. 2(a)), the average size of the largest SIA clusters is limited to less than 10 atoms only. However, the average size of the largest SIA clusters above the transition energy rapidly increases up to 40, 157 and 308 SIAs in 100, 200 and 300 keV collision cascades, respectively. The number of SIA clusters containing more than 14 SIAs is close to zero below the transition energy, whereas this quantity also rapidly increases above this energy (Fig. 2(b)). Therefore, the dependences of both the average size of the largest SIA clusters and the number of SIA clusters containing more than 14 SIAs on E_{PKA} indicate that large SIA clusters are present after the transition energy, similar to the results reported by Setyawan et al. [22].

For the binary W−Re system with 5 and 10 at.% Re, N_{FP} produced with E_{PKA} of 100, 200 and 300 keV also increases with E_{PKA}, and the slope of the curve is identical with the data obtained using pure W. Therefore, the effects of randomly distributed substitutional Re atoms on the number of surviving defects can be ignored because of the slight mass difference between the W and Re atoms. Similar results have also been observed in Fe−Cr alloys [48].

3.2. Defect clustering

In the present simulations, three typical defect distributions are observed in pure W and W−Re alloys, namely, unfragmented, unconnected and connected, according to the criterion suggested in Ref. [49]. By considering the W−Re alloys as an example, Fig. 3 denotes three typical defect distributions, induced by the 300 keV cascade at the peak damage state. Most of the high-energy cascades at peak stages belong to unfragmented cases, where the cascade appears in a locally compact region, producing a massive and unbroken molten region (Fig. 3(a)). Fig. 3(b) depicts a case of clear fragmentation, separated into three unconnected subcascades. Fig. 3(c) illustrates the continuous morphology of the fragmentations through the connected subcascades. According to a statistical analysis, when E_{PKA} is less than 100 keV, the probability for a cascade to split into subcascades is close to zero. When E_{PKA} is 200 and 300 keV, the probabilities of the subcascades increase to approximately 20% and 30%, respectively. These results indicate the
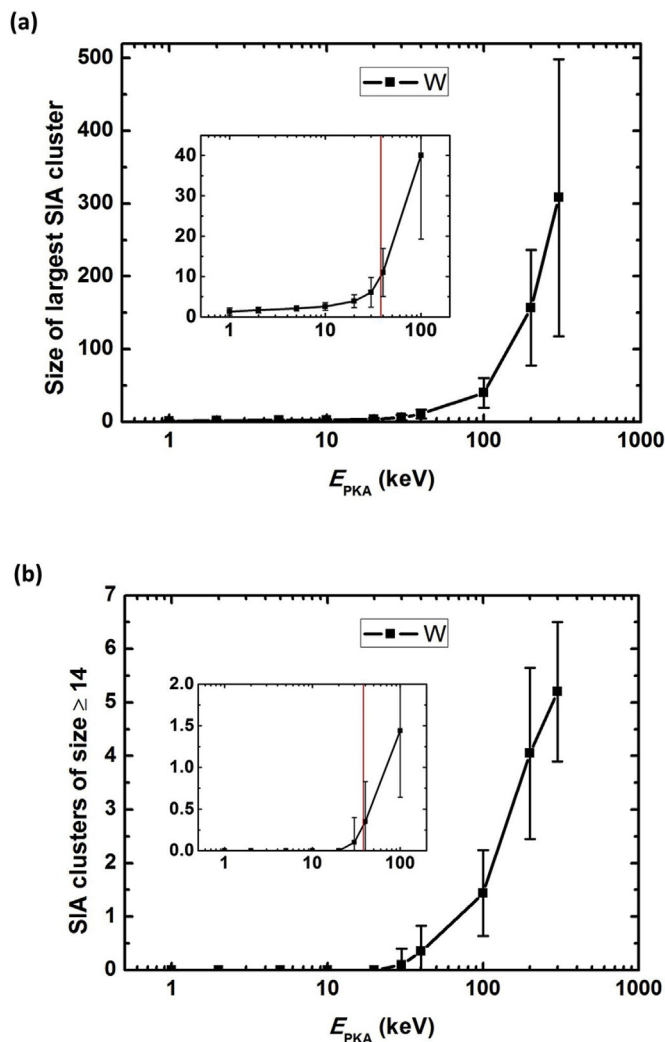

Fig. 2. (Color online) Energy dependence of the (a) average size of the largest SIA clusters and (b) number of SIA clusters with size ≥ 14 per cascade in pure W, as a function of PKA energy. The red solid line represents the transition energy (38 keV). The error bars denotes the average standard errors. (For interpretation of the references to color in this figure legend, the reader is referred to the Web version of this article.)

existence of a critical E_{PKA} for the subcascades' appearance. Previous studies [24,50,51] have demonstrated that this critical energy is close to 150 keV for W. The number of connected subcascades increases when E_{PKA} increases, which is in agreement with the behaviour observed in pure Fe based on the high-energy cascade simulations of Zarkadoula et al. [52].

Fig. 4(a) and 4(c) show the typical defect distribution in pure W and W−10 at.% Re alloys 100 ps after the bombardment in cascades when $E_{PKA} = 300$ keV. Large interstitial clusters are accompanied by the formation of large vacancy clusters, exhibiting a three-dimensional shape (cavity), whereas the large interstitial clusters mainly exhibit a two-dimensional platelet shape (loops). According to the present simulation results, most of the large interstitial clusters and free interstitial dumbbells have configurations containing Re atoms in W−10 at.% Re system, which is different from the case obtained for pure W. According to a statistical analysis, the atomic percentage of Re atoms in the final stable defects is approximately up to 10% and 15% in W−5 at.% Re and W−10 at.% Re alloys, respectively, which are higher than the average Re
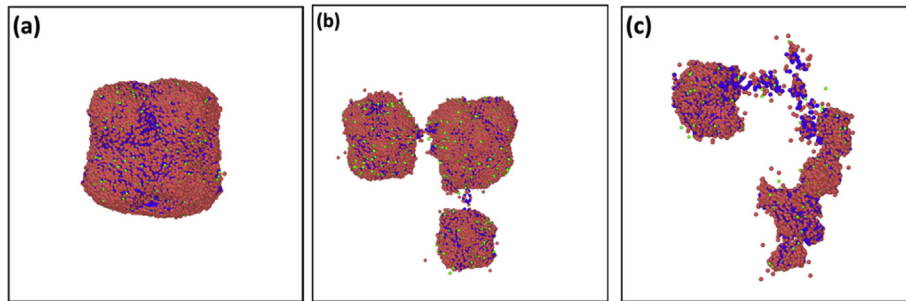
Fig. 3. (Color online) Snapshots of three representative cascades at the peak damage states in W—Re alloys: (a) unfragmented type, (b) unconnected type and (c) connected type. The blue, reddish and green balls represent the vacancies, W interstitials and Re interstitials, respectively. (For interpretation of the references to color in this figure legend, the reader is referred to the Web version of this article.)
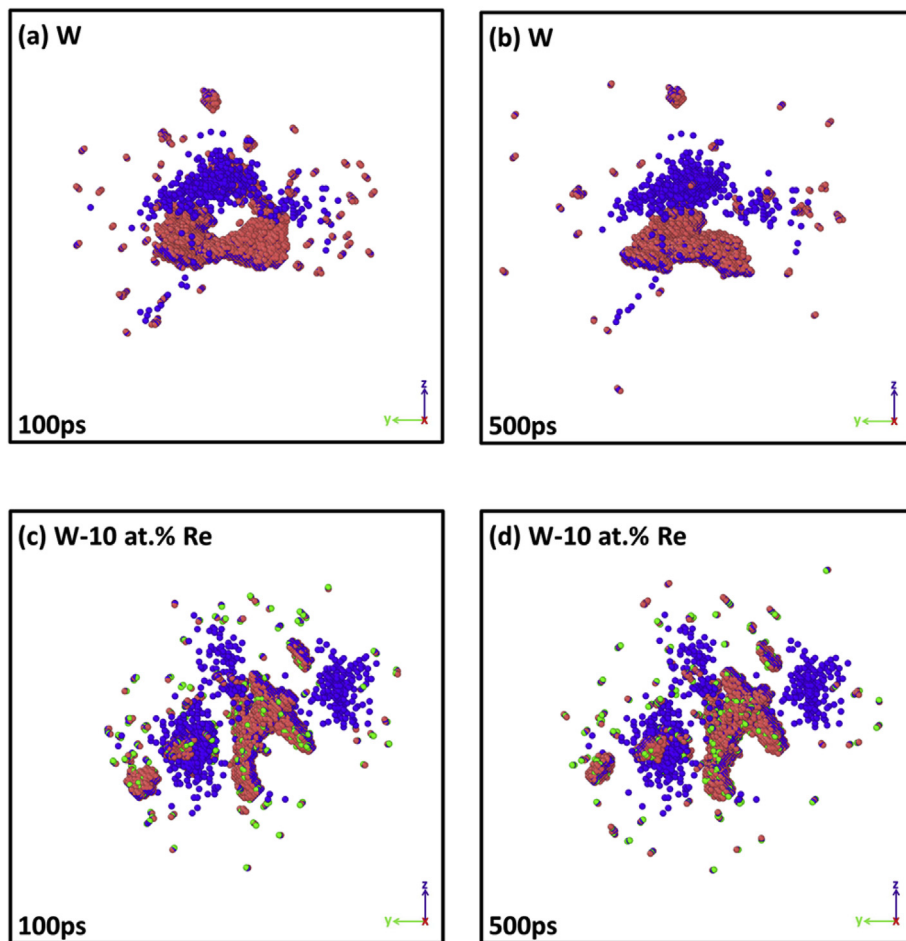

Fig. 4. (Color online) Typical defects distribution after the bombardment of 300 keV cascades at 300 K (at 100 ps in pure W (a) and W—10 at.% Re alloys (c)) and then further relaxed at 1000 K (at 500 ps in pure W (b) and W—10 at.% Re alloys (d)). The color representation is the same as for Fig. 3. (For interpretation of the references to color in this figure legend, the reader is referred to the Web version of this article.)

concentration in the alloy. Thus, the cascades clearly induce the local enrichment of Re atoms in the W—Re system. A similar phenomenon has also been observed and explained in the Fe—Cr system [53,54]. The possible reason for the high Re percentage in defects is the high binding energy of the interstitial defect both with interstitial and substituted Re atoms [27]. Thus, the SIAs and their clusters generated in cascade displacements are attractive to the Re atoms in the W—Re alloy systems, and such an attraction suppresses their migration. Furthermore, the migration energy and rotation energy of a mixed W—Re dumbbell are low [27]. Hence, the

W—Re dumbbell far from the interstitial clusters can also be absorbed through a long-time diffusion process, resulting in the local segregation of the Re atoms.

The average number of defect clusters and the size of the largest clusters formed by the cascades after 100 ps are also analysed, as summarised in Table 4. The results indicate that the average number of vacancy and interstitial clusters and the largest size of the formed clusters of point defects significantly increase with an increase in E_{PKA}. It can be observed that the effects of the substitutional Re atoms on the aforementioned quantities are limited. In

Table 4
Average number of vacancy clusters with size ≥ 3 (N_{vac}) and interstitial clusters with size ≥ 4 (N_{int}) and the average number of interstitial clusters containing Re atoms (N_{int}^{Re}). The values in brackets denote the standard errors after 30 events for each simulation. The largest vacancy (S_{vac}^{max}) and interstitial (S_{int}^{max}) clusters that we observed in each set of 30 simulation events are presented in the last two columns and are determined using the net defect count (the difference between the number of interstitials and the number of vacancies).

E_{PKA} (keV)	Re (at.%)	N_{vac}	N_{int}	N_{int}^{Re}	S_{vac}^{max}	S_{int}^{max}
100	0	3(2)	4(1)	n/a	160	120
	5	4(2)	4(1)	3(1)	146	177
	10	5(2)	4(1)	3(1)	199	194
200	0	9(4)	7(2)	n/a	347	351
	5	8(4)	7(2)	5(1)	335	369
	10	11(4)	7(2)	6(2)	496	552
300	0	15(5)	9(3)	n/a	713	755
	5	10(5)	10(2)	7(2)	676	562
	10	15(5)	9(3)	8(3)	710	735

Fig. 5. (Color online) Fraction of (a) vacancies in clusters with size more than 3 and (b) interstitials in clusters in clusters with size more than 4, as a function of PKA energy for cascades in pure W, W−5 at.% Re and W−10 at.% Re alloys, respectively. The error bars denotes the average standard errors. (For interpretation of the references to color in this figure legend, the reader is referred to the Web version of this article.)

addition, it should be noted that 70%−90% of the interstitial clusters contain Re atoms. Hence, the configurations of these interstitial clusters during the subsequent long-time annealing or ageing evolution after the cascades may be influenced by the segregation of the Re atoms in these clusters. A recent study conducted by our group shows that the mobility of these interstitial clusters containing Re atoms was substantially suppressed when compared with the mobility of the pure W interstitial cluster [55]. This low mobility reduces the likelihood of interaction and merging between interstitial clusters or interstitial dislocation loops. Eventually, it may result in a greater number density and a smaller size of interstitial dislocation loops in the W−Re system when compared with those in pure W. In addition, these Re-containing interstitial clusters may provide nucleation positions for the irradiated precipitate phase because of their large binding energy to Re atoms and the rapid three-dimensional motion of the W−Re mixed dumbbell. Thus, the growth of these clusters after long-term evolution may facilitate the formation of the Re phase, whose effects have been reviewed elsewhere [10−14].

Fig. 5 depicts the fraction of the clustered vacancies and interstitials as the E_{PKA} function. Here, such a fraction is defined as the ratio of the number of interstitial (vacancies) atoms in the clusters (with at least three vacancies or four interstitials) to the total number of interstitials (vacancies) atoms, which is the sum of defect atoms in both the free and cluster states. As denoted in the figure, as E_{PKA} increases, the fractions of clustered vacancies and interstitials in bulk W and randomly substituted W−Re alloys also increase within the statistical uncertainties. The value of the clustered vacancy fraction in the alloys and pure W is between 0.2 and 0.5. Furthermore, the interstitial fraction in the clusters is higher than that in the vacancies with a value between 0.4 and 0.8. These fractions are also obtained using the predicted model of W [56]. Fig. 6 presents the detailed size distributions of the interstitial and vacancy clusters obtained with different PKA energies in pure W and with W−5 at.% Re and W−10 at.% Re alloys. Our results revealed that the dominant clusters (sizes of 3−10 for vacancy clusters and 4−50 for interstitial clusters) in all the three systems are small, as depicted in Fig. 6. Note that the number of large clusters is slightly less in pure W when compared those in W−Re alloys for E_{PKA} of 100 and 200 keV, whereas it is slightly higher in pure W than those in W−Re alloys in the 300 keV cascades. Although the observed phenomena in the 300 keV collision cascades are in agreement with the experimental results [57], the Re effect on the cluster size is not evident within a time scale of 100 ps from the entire perspective. The possible reason is that the ZBL function is used for short distance interactions in both W and Re. Meanwhile, the
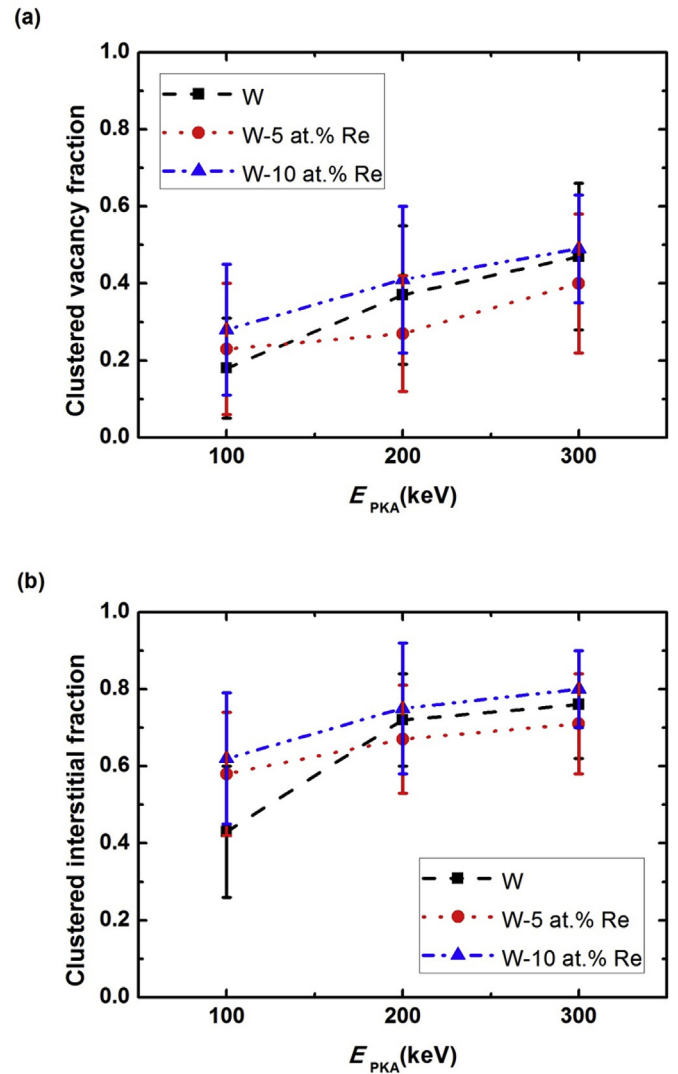
effects of Re atoms on the cluster size may be limited by the number of simulation events and the time scale of 100 ps; additional data and long-time scale are probably necessary to establish a general trend.

To better understand the effects of substitutional Re atoms on the subsequent evolution of defect clusters, the systems obtained 100 ps after the bombardment of 300 keV cascades are relaxed at high temperatures of 1000 K for 500 ps using the NVT ensemble with a time step of 1 fs. Fig. 4(b) and (d) denote the system snapshots 500 ps after the bombardment of pure W and W−10 at.% Re at 1000 K, respectively. During this process, the vacancies remain immobile, similar to the results obtained at low temperatures. However, a difference is observed in the evolution of the surviving interstitials in case of the alloy and pure W systems. As depicted in the figures, most of the interstitial clusters and W−W dumbbells migrate rapidly and combine to form larger clusters in pure W. In addition, several W−W dumbbells do not combine with the clusters but instead move from the centre to the periphery of the cluster. The complete movie is presented in the Supplementary
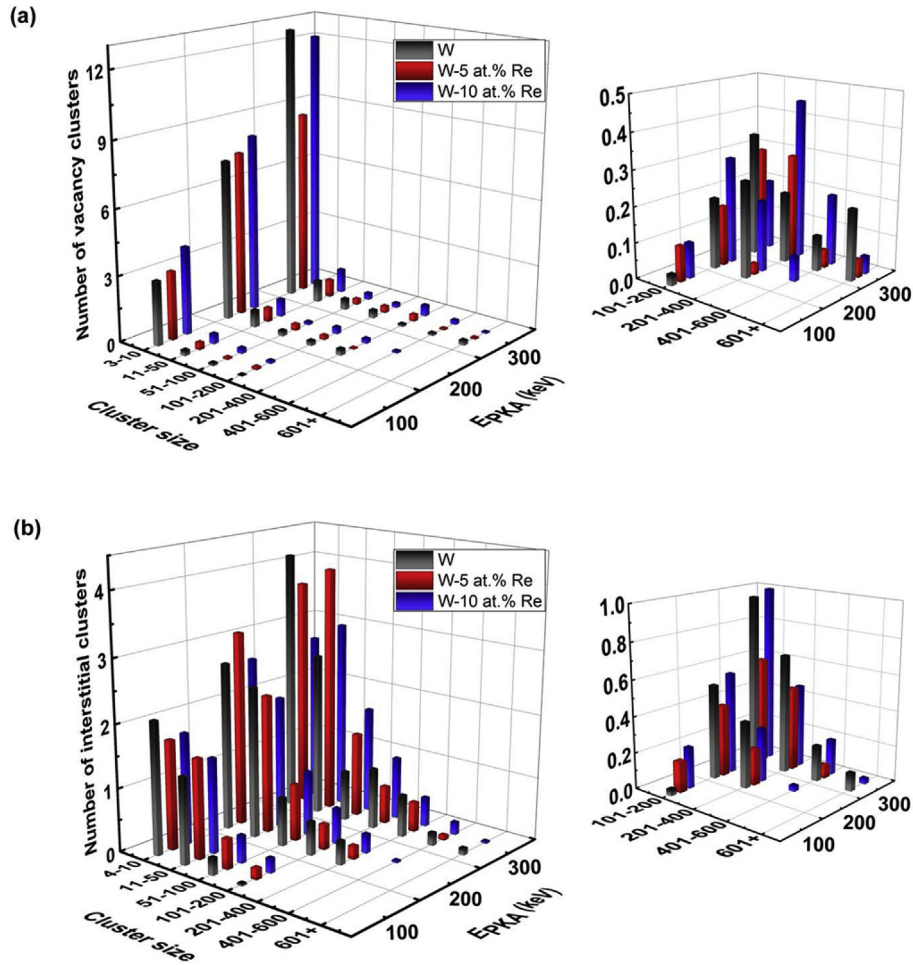
Fig. 6. (Color online) Cluster size distribution for three or more vacancies (a) and four or more interstitials (b) produced by PKA energies between 100 keV and 300 keV of pure W, W−5 at.% Re and W−10 at.% Re alloys, respectively. Each data is calculated from the average of 30 cascade events. (For interpretation of the references to color in this figure legend, the reader is referred to the Web version of this article.)

material (Fig. 4-ab-movie.mov). Different from the results in pure W, the interstitial clusters containing Re atoms and Re−Re dumbbell migrate slowly in W−10 at.% Re alloys even after long-time high-temperature relaxations. Thus, noticeable differences are not observed between Fig. 4(c) and (d). The related movie has been provided in the Supplementary material (Fig. 4-cd-movie.mov). All these results indicate the pinning effect of Re atoms on the movement of interstitial clusters, which agrees with the results of Chen et al. [55]. Therefore, although the Re effect on cluster size is not observed within a time scale of 100 ps, in case of long-time scale, the restriction of the long-range diffusion of the SIA clusters by Re atoms reduces the possible interaction between the interstitial clusters. This may result in the formation of smaller size and larger number density interstitial clusters in the W−Re system when compared with those formed in the pure W system, similar to the experimental results [57].

3.3. Dislocation loop structure

In this study, each large defect cluster has been analysed to determine the properties of the dislocation loops. Table 5 presents the number of interstitial dislocation loops. We observed that most of the interstitial dislocation loops have the Burgers vector $b = 1/2<111>$. The remaining loops have either $b = <100>$ or take the form of mixed loops with Burgers vectors of $1/2<111>$ and $<100>$.

Table 5
Statistical results of different types of interstitial loops. 'Mixed loop' denotes a mixture of $1/2<111>$ and $<100>$ loops. 'Total' denotes the total of three types of interstitial loops. These data are based on 30 cascade events for each condition.

E_{PKA} (keV)	Re (at.%)	$1/2<111>$	$<100>$	Mixed loop	Total
100	0	50	0	1	51
	5	63	0	1	64
	10	64	0	5	69
200	0	100	0	10	110
	5	99	0	5	104
	10	103	0	13	116
300	0	136	1	18	155
	5	159	0	15	174
	10	170	0	20	190

These results are consistent with the recent experiments [58] and MD simulations [22,24,26] of irradiated W. However, we noticed that $<100>$ interstitial loops are the only ones observed after the bombardment of 300 keV cascades in pure W. This observation is different from the previous works [24] that used E_{PKA} of 150 keV in pure W simulated with the DD07 potential [45], where almost half of the small interstitial loops take the Burgers vector $b = <100>$. This can be attributed to the DD07 potential, which predicted the $<100>$ loops rather than the $1/2<111>$ loops as the stable dislocation loop states (refer to Ref. [27] for a review).

Fig. 7 illustrates the detailed size distributions of the interstitial loops after the cascades with different PKA energies in pure W, W−5 at.% Re and W−10 at.% Re alloys. With an increase in E_{PKA}, the number of large loops in W is slightly higher than that of the W−Re alloys; however, the overall difference is insignificant. Based on Table 5, the total number of interstitial loops generated after the 100 and 300 keV collision cascades increase with increasing Re concentration from 0 to 10 at.%. However, the number of interstitial loops formed in the 200 keV collision cascades in W−10 at.% Re
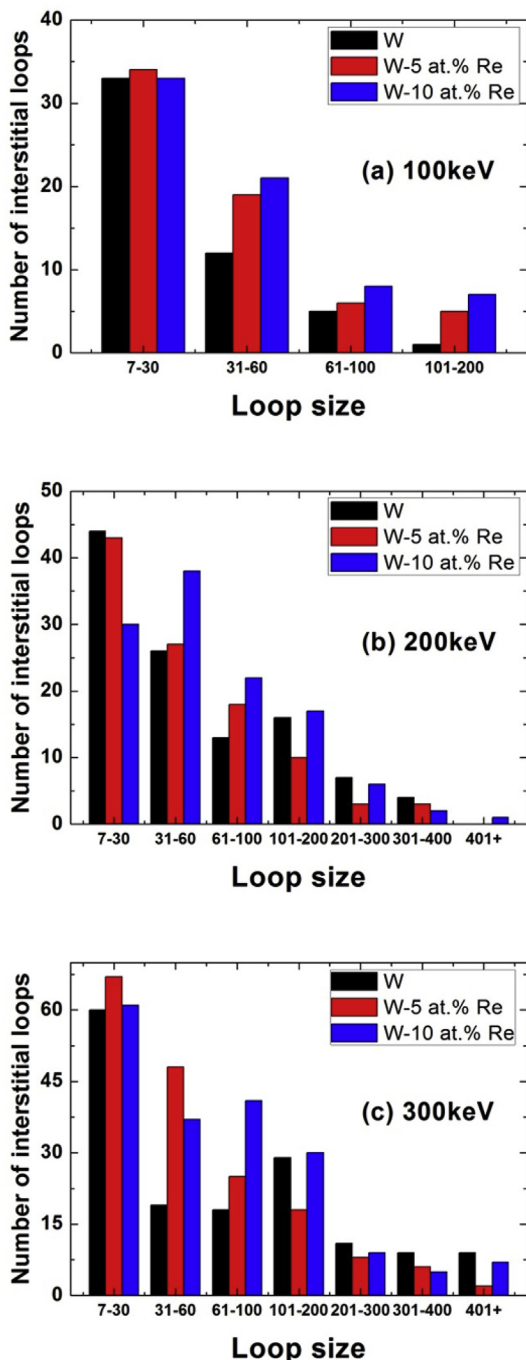
Fig. 7. (Color online) Size distribution of interstitial loops formed in pure W, W−5 at.% Re and W−10 at.% Re alloys after (a) 100 keV, (b) 200 keV and (c) 300 keV cascades. Each data is calculated from the sum of 30 cascade events. (For interpretation of the references to color in this figure legend, the reader is referred to the Web version of this article.)

alloy reaches the maximum value and attains the minimum value in W−5 at.% Re alloy among the three chemical compositions. Previous experimental results [58] indicated that a larger number density and smaller average size distribution were found in W−Re alloys when compared with those in pure W because the Re atoms suppress the growth of loops, which is consistent with our results in case of the 300 keV cascades. However, considering that the results obtained in the 100 and 200 keV cascades do not completely follow this trend, the effects of Re atoms on the number and size distribution of interstitial loops are also considered to be limited at the initial radiation stage within a 100-ps time scale. The possible reasons are as follows: (1) the results of the experiment are based on high-dose irradiation and high irradiation temperature (500 °C), which is different from the present cases (one single cascade and low simulation temperature at 300 K); (2) in our simulations, only the randomly substituted solid solution W−Re alloys have been investigated, different from the experimental samples with the presence of Re in various states and forms; (3) in the experiments, low-energy ion irradiation results in the thickness of injection limited within several hundred angstroms; thus, the surface effect may influence the radiation defect evolution; and (4) considering that the large box in this study contains up to several tens of millions of atoms, the results may be limited by the number of simulation events and the time scale of the MD simulations. Hence, additional data may be required to deduce the general trend. Furthermore, we observed that small SIA clusters in pure W are more likely to be mobile and combine forming larger SIA clusters than that formed in the W−Re system, with an increase in simulation time and temperature (Fig. 4). Therefore, if the simulation time could be increased, then the average size of the interstitial loops may also increase and the number density in pure W decreases, obtaining the same results as those obtained in the experiments [58].

Figs. 8 and 10 depict the snapshots of the dislocation loops at different cascade stages with $E_{PKA} = 300$ keV in pure W and W−10 at.% Re alloys, respectively. Fig. 8(a) illustrates the cascade at peak damage with the appearance of a few interstitial-type 1/2<111> segments. Subsequently, the interstitial-type <100> segments are formed. With an increase in the simulation time, both the 1/2<111> and <100> segments increase, which is also accompanied by recovery through the diffusion and recombination processes (Fig. 8(b)). In addition, the direct formation of five completed interstitial dislocation loops is observed outside the cascade centre (Fig. 8(c)). In this figure, these loops can be divided into three different groups. (1) The single loop that have the same properties as the loop formed after the low-energy cascade, e.g., loop-1 in Fig. 8(c), (2) the loop that employs the same Burgers vector but located on different habit planes, as shown by the example of loop-2 in Fig. 8(c). Fig. 9(a) and (b) denote the {111} habit plane of the upper section of loop-2, and Fig. 9(c) and (d) illustrate the {110} habit plane of the bottom section of loop-2. The schematic of this loop is shown by the inserted image in Fig. 9. Therefore, the angle between the two habit planes can be determined to be 26.81°. The reasons for the formation of such loop may be based on two different mechanisms as follows. The first reason may be the loop interaction that occurs between two loops. Previous studies [59−61] have confirmed that the interaction between the prismatic loops may not follow the conservation law of Burgers vector; thus, the formation of such a loop configuration is reasonable. The second one is the effects induced by the shockwave from the high-energy cascades. The existence of shockwaves in the high-energy cascade has been confirmed previously [47,62]. Further, Setyawan et al. [47] showed that the high-energy cascade is sufficient to induce multiple supersonic shockwaves, which are closely interconnected in W, resulting in the formation of large interstitial
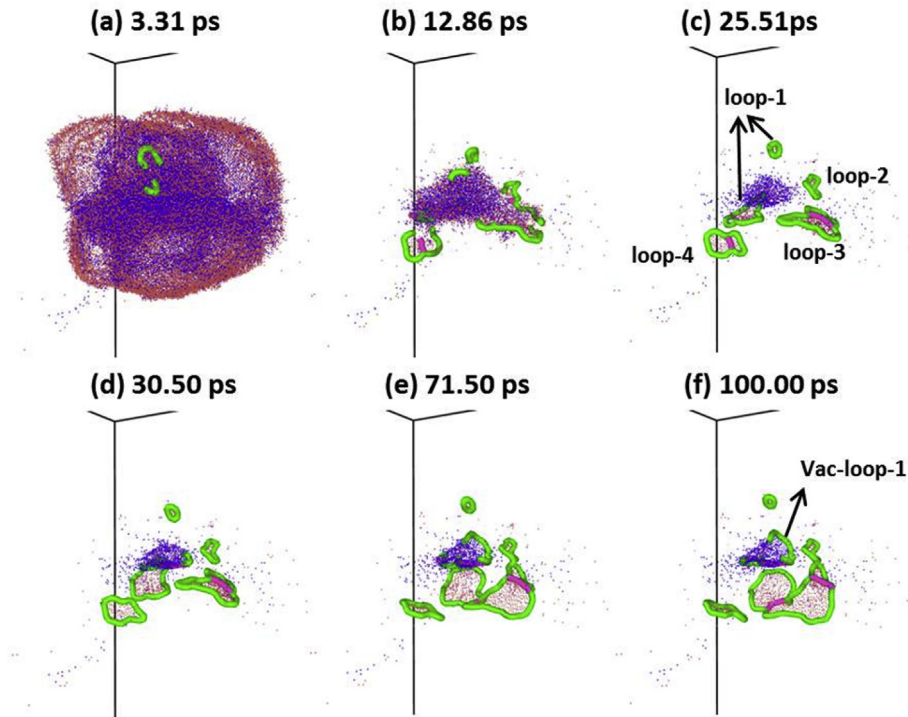
Fig. 8. (Color online) Dislocation loop evolution for 300 keV cascades in pure W. The reddish and blue dots represent W interstitials and vacancies, respectively. The green lines represent the 1/2<111> segments, whereas the pink lines represent the <100> segments. Here we used OVITO software [42] to visualize the dislocation loop evolution. (For interpretation of the references to color in this figure legend, the reader is referred to the Web version of this article.)
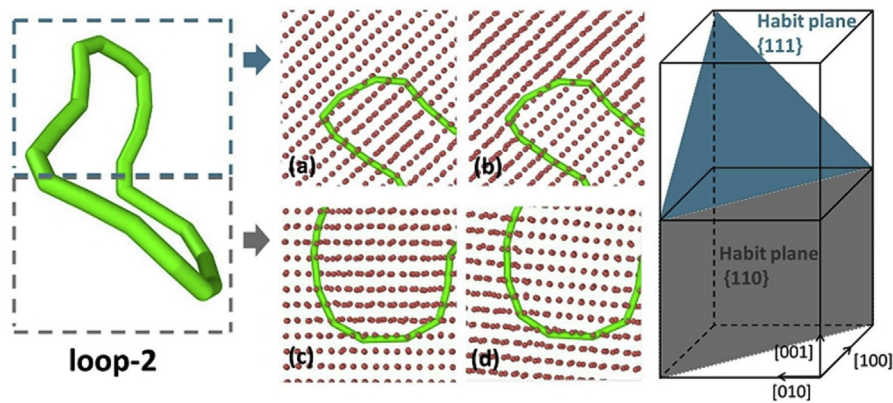
Fig. 9. (Color online) The habit planes of the loop-2: (a) & (b) {111}, (c) & (d) {110}. The inset shows the schematic of two habit plane. The difference between (a) & (b) or (c) & (d) is due to a small angle deviation in the arrangement of atoms inside and outside the loop-2. (For interpretation of the references to color in this figure legend, the reader is referred to the Web version of this article.)

clusters and affecting the loop formation mechanism. Given the aforementioned explanation and considering the high PKA energy, we speculate that multiple shockwaves from the high-energy cascade in this work may contribute to this defect configuration, which would be investigated in our future work. (3) The third loop is a mixed loop with various dislocation segments (loop-3 and loop-4 in Fig. 8(c)), which are considered to be from the loop–loop and loop dislocation reaction, as indicated in Fig. 8(b) and (c). Although the initial computational box does not include a dislocation line before the cascade simulations, the dislocation network can also be formed during the cascade process by the evolution of vacancy clusters and loops, as stated in the following text. Thus, a loop dislocation reaction is also possible, as indicated by the

present study. With further evolution, the number of defects becomes almost constant, and the vacancy-type 1/2<111> and <100> segments can be observed (Fig. 8(d)). From Fig. 8(d), it can also be observed that the segments of <100> loop in loop-4 have disappeared. At approximately 41 ps, two 1/2<111> loops move owing to the effect of elastic interaction and then combine to form a large mixed loop (Fig. 8(e)), possibly due to the loop–loop reaction. Note that such a mixed loop still has different habit planes with the same Burgers vector and that the types are more complex. The new {100} habit plane is also observed for the 1/2<111> loop segment, as reported for Fe by Gao et al. [61]. Fig. 8(f) shows two interstitial 1/2<111> loops and a mixed loop with a total length of 65 nm, but the vacancy loops are still not completely formed.
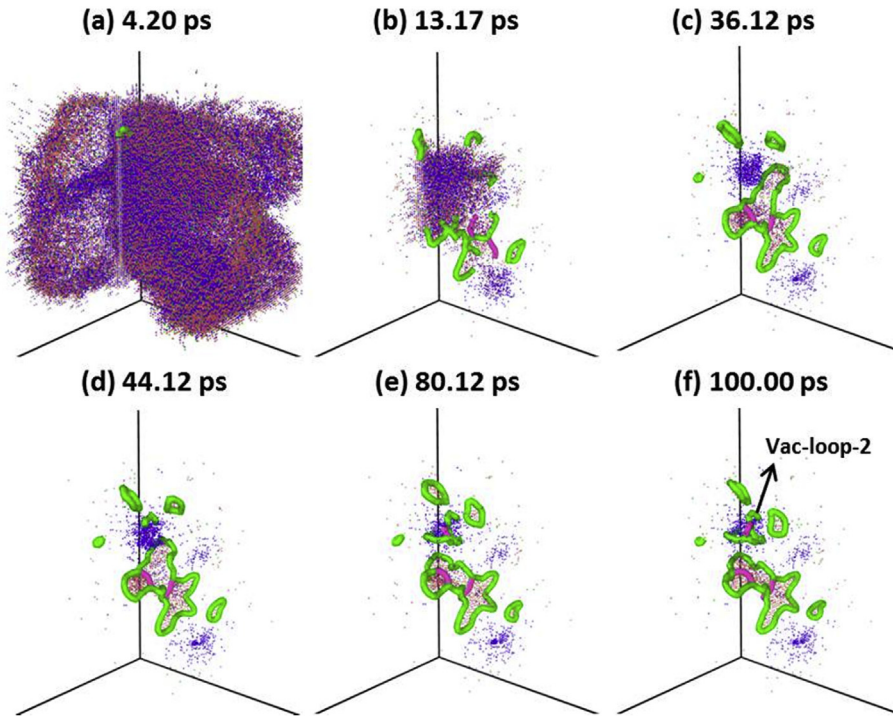
Fig. 10. Dislocation loop evolution for 300 keV cascades in W−10 at.% Re alloys. The green dots represent Re interstitials, and others color representation are the same as for Fig. 8. (For interpretation of the references to color in this figure legend, the reader is referred to the Web version of this article.)

Fig. 10 depicts the evolution of the cascade in W−10 at.% Re alloys similar to pure W; that is, several interstitial-type dislocation loops are formed and can also be divided into three groups, as explained previously. The vacancy-type segments also begin to appear even though complete loops are not formed after the simulations. However, different from the case of high-energy cascades in pure W, the interactions of loops have a low probability to occur in W−10-at.% Re alloys (Fig. 10(d)−10(f)). The detailed analysis of

the loops denotes the enrichment of Re atoms in the loop core. Thus, the pinning effect induced by the segregation of these Re atoms has induced the low mobility of the interstitial $1/2<111>$ loops in W−Re alloy, as discussed in Ref. [55], decreasing the interaction probability among different loops.

In the present simulations, the $1/2<111>$ and mixed $1/2<111>−<100>$ interstitial dislocation loops are observed in pure W and W−Re solid solution alloys with 5 and 10 at.% Re. However, only a single $<100>$ interstitial dislocation loop (with 24 interstitials) is observed within the cascade with E_{PKA} of 300 keV in pure W (Fig. 11(a)), which is not observed in the W−Re alloy systems. This single $<100>$ interstitial loop observed in this study is directly formed during the cooling of the cascade melt from a collection of interstitial atoms and is stable within a time scale of 100 ps. The largest interstitial-type dislocation loop observed in pure W (Fig. 11(b)) and W−Re alloys (Fig. 12(a)) contains 755 and
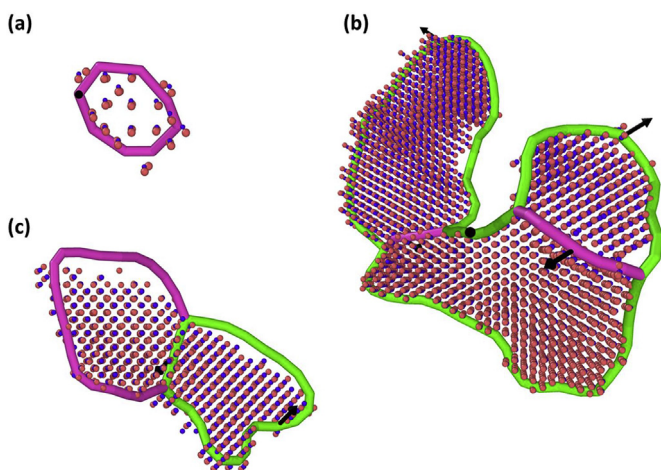

Fig. 11. (Color online) (a) A $<100>$ interstitial loop observed within a cascade with a PKA energy of 300 keV in pure W, consisting of 24 interstitials (net defect number). (b) The largest interstitial loop in pure W, consisting of 755 interstitials. (c) A mixed interstitial loop with a Burgers vector of $1/2<111>$ and $<100>$, as viewed along the $<100>$ direction in pure W, consisting of 247 interstitials. The blue (small) and reddish (large) balls represent the vacancies and W interstitials, respectively. The green lines represent the $1/2<111>$ segments, whereas the pink lines represent the $<100>$ segments. (For interpretation of the references to color in this figure legend, the reader is referred to the Web version of this article.)
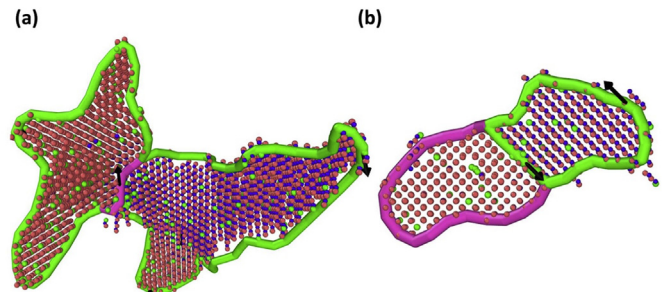

Fig. 12. (Color online) (a) The largest interstitial loop in W−Re alloys, consisting of 735 interstitials. (b) A mixed interstitial loop with a Burgers vector of $1/2<111>$ and $<100>$, as viewed along the $<100>$ direction in W−Re alloys, consisting of 234 interstitials. The green balls represent Re interstitials, and others color representation are the same as for Fig. 11. (For interpretation of the references to color in this figure legend, the reader is referred to the Web version of this article.)
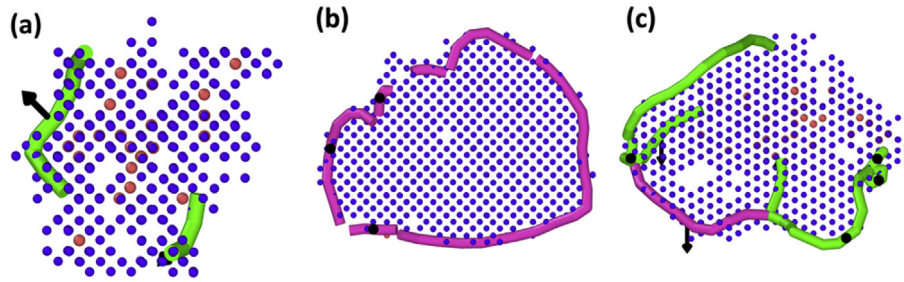
Fig. 13. (Color online) Three typical open vacancy loop structures; (a) A 366-vacancy cluster with the 1/2<111> segments; (b) A 591-vacancy cluster with the <100> segments; (c) A 679-vacancy cluster with the mixed 1/2<111>−<100> segments. All of them are viewed along the <100> direction. The color representation is the same as for Fig. 11. (For interpretation of the references to color in this figure legend, the reader is referred to the Web version of this article.)

735 interstitials, respectively. Both of them are mixed 1/2<111>−<100> interstitial loops, mainly comprising a set of <111> crowdions and <100> dumbbells. However, the formation mechanisms of these two loops differ. The largest interstitial loop in pure W is formed by combining a moving 1/2<111> interstitial loop with a mixed 1/2<111>−<100> interstitial loop formed directly during cascade cooling. However, the largest interstitial loop in W−Re alloys is formed directly during cascade cooling. Fig. 11(c) shows that a mixed interstitial loop contains 247 interstitials in pure W, with 1/2<111> and <100> loops being of the same length. As depicted in Fig. 12(b), a similar interstitial loop structure is observed in W−Re alloys. In Figs. 11(c) and 2(b), both the 1/2<111> and <100> dislocation segments are formed at approximately the same time during cascade cooling. Both the dislocation segments apparently maintain their Burgers vectors until the end of the MD run, resulting in a mixed 1/2<111>−<100> interstitial loop. Determining whether this loop eventually transforms into a <100> or a 1/2<111> loop will require a considerably longer time. In Fe and FeCr, the mixed interstitial 1/2<111>−<100> loops were previously shown to be transformed into a complete <100> loop in the massively overlapping cascades [63].

Apart from the interstitial dislocation loops, a complete vacancy dislocation loop has not been observed in pure W or random W−Re alloys with 5 and 10 at.% Re systems, which is similar to the results of pure W reported in Refs. [24,26]. Meanwhile, the results of Setyawan at el [22]. indicated the formation of complete vacancy <100> loops. The difference may be due to the different simulation temperatures and potentials applied for the cascade simulations [24]. Although the complete vacancy dislocation loops are not observed in the present simulations, vacancy clusters and incomplete vacancy loops are evident at the centre of the cascades, as shown by the Vac-loop-1 in Fig. 8(f) and Vac-loop-2 in Fig. 10(f). These incomplete vacancy loops are analysed using the OVITO and DXA. According to this analysis method, if the loop consists of vacancy clusters but is not completely closed, then the loop is referred to as incomplete vacancy loop. Thus, in this study, incomplete vacancy loop can also be defined as an open vacancy loop. We have observed three different types of open vacancy loops in pure W and W−Re alloys with 5 and 10 at. % Re as follows: 1/2<111>, <100> and mixed 1/2<111>−<100> segments, which are dominated by <100> segments (60%), followed by mixed 1/2<111>−<100> (30%) and 1/2<111> (10%) segments. Fig. 13 shows the three typical structures of the open vacancy loops. Here, the 1/2<111>, <100> and mixed 1/2<111> and <100> segments have defect numbers of 366, 591 and 679, respectively. The figure also illustrates that the size of the open vacancy loops formed by the mixed segments is slightly large and that these loops tend to form a highly complex dislocation network.

4. Conclusion

High-energy displacement cascades of up to 300 keV recoil energy have been simulated through MDs in pure W and random W−Re alloys with 5 and 10 at.% Re. The following conclusions can be obtained based on the results:

(1) In the case of pure W, the number of FPs increases gradually with the increasing PKA energy, which ranges from 1 to 300 keV, and presents two schemes of power law. These two schemes intersect at a transition energy that occurs at approximately 38 keV.
(2) The presence of randomly distributed 5 and 10 at.% Re atoms does not affect either the number of surviving defects or their clustered fraction. However, it potentially leads to the local enrichment of Re atoms in the W−Re system. This feature may drastically reduce the interstitial cluster mobility in W−Re when compared with pure W.
(3) The interstitial-type dislocation loops are dominated by the 1/2<111> loops, and the formation of the mixed 1/2<111>−<100> loops is also observed. However, no complete vacancy-type dislocation loops are formed.
(4) High-energy cascade induces a unique loop configuration that a loop takes the same Burgers vector but located on various habit planes.
(5) The pinning effect induced by the segregation of Re atoms leads to slow mobility of the interstitial 1/2<111> loops in the W−Re alloy, thereby suppressing the growth of loops.

Acknowledgements

Appendix A. Supplementary data

Supplementary data to this article can be found online at https://doi.org/10.1016/j.jnucmat.2019.06.027.

References

[1] H. Bolt, V. Barabash, W. Krauss, et al., Materials for the plasma-facing components of fusion reactors, J. Nucl. Mater. 329−333 (2004) 66−73.
[2] R. Neu, V. Bobkov, R. Dux, et al., Final steps to an all tungsten divertor tokamak, J. Nucl. Mater. 363−365 (2007) 52−59.
[3] K. Wittlich, T. Hirai, J. Compan, et al., Damage structure in divertor armor materials exposed to multiple ITER relevant ELM loads, Fusion Eng. Des. 84

(2009) 1982—1986.

[4] G. Federici, C.H. Skinner, J.N. Brooks, et al., Plasma-material interactions in current tokamaks and their implications for next step fusion reactors, Nucl. Fusion 41 (2001) 1967.

[5] G.A. Cottrell, R. Pampin, N.P. Taylor, Transmutation and phase stability of tungsten armor in fusion power plants, Fusion Sci. Technol. 50 (2006) 89—98.

[6] M.R. Gilbert, J.C. Sublet, Neutron-induced transmutation effects in W and W-alloys in a fusion environment, Nucl. Fusion 51 (2011), 043005.

[7] Y. Nemoto, A. Hasegawa, M. Satou, et al., Microstructural development of neutron irradiated W-Re alloys, J. Nucl. Mater. 283—287 (2000) 1144—1147.

[8] T. Tanno, A. Hasegawa, J.C. He, et al., Effects of transmutation elements on the microstructural evolution and electrical resistivity of neutron-irradiated tungsten, J. Nucl. Mater. 386—388 (2009) 218—221.

[9] M. Fukuda, K. Yabuuchi, S. Nogami, et al., Microstructural development of tungsten and tungsten-rhenium alloys due to neutron irradiation in HFIR, J. Nucl. Mater. 455 (2014) 460—463.

[10] T. Tanno, M. Fukuda, S. Nogami, et al., Microstructure development in neutron irradiated tungsten alloys, Mater. Trans. 52 (2011) 1447—1451.

[11] A. Hasegawa, M. Fukuda, T. Tanno, et al., Neutron irradiation behavior of tungsten, Mater. Trans. 54 (2013) 466—471.

[12] A. Hasegawa, M. Fukuda, S. Nogami, et al., Neutron irradiation effects on tungsten materials, Fusion Eng. Des. 89 (2014) 1568—1572.

[13] M. Fukuda, T. Tanno, S. Nogami, et al., Effects of Re content and fabrication process on microstructural changes and hardening in neutron irradiated tungsten, Mater. Trans. 53 (2012) 2145—2150.

[14] T. Tanno, A. Hasegawa, J.C. He, et al., Effects of transmutation elements on neutron irradiation hardening of tungsten, Mater. Trans. 48 (2007) 2399—2402.

[15] Q. Xu, T. Yoshiie, H.C. Huang, Molecular dynamics simulation of vacancy diffusion in tungsten induced by irradiation, Nucl. Instrum. Methods Phys. Res., Sect. B 206 (2003) 123—126.

[16] M.J. Caturla, T.D.D.L. Rubia, M. Victoria, et al., Multiscale modeling of radiation damage: applications to damage production by GeV proton irradiation of Cu and W, and pulsed irradiation effects in Cu and Fe, J. Nucl. Mater. 296 (2001) 90—100.

[17] N.Y. Park, Y.C. Kim, H.K. Seok, et al., Molecular dynamics simulation of irradiation damage in tungsten, Nucl. Instrum. Methods Phys. Res., Sect. B 265 (2007) 547—552.

[18] J. Fikar, R. Schäublin, Molecular dynamics simulation of radiation damage in bcc tungsten, J. Nucl. Mater. 386—388 (2009) 97—101.

[19] C. Björkas, K. Nordlund, S. Dudarev, Modelling radiation effects using the ab-initio based tungsten and vanadium potentials, Nucl. Instrum. Methods Phys. Res., Sect. B 267 (2009) 3204—3208.

[20] T. Troev, N. Nankov, T. Yoshiie, Simulation of displacement cascades in tungsten irradiated by fusion neutrons, Nucl. Instrum. Methods Phys. Res., Sect. B 269 (2011) 566—571.

[21] B. Fu, B. Xu, W. Lai, et al., Computer simulation of displacement cascades in tungsten with modified F—S type potential, J. Nucl. Mater. 441 (2013) 24—28.

[22] W. Setyawan, G. Nandipati, K.J. Roche, et al., Displacement cascades and defects annealing in tungsten, Part I: defect database from molecular dynamics simulations, J. Nucl. Mater. 462 (2015) 329—337.

[23] M. Warrier, U. Bhardwaj, H. Hemani, et al., Statistical study of defects caused by primary knock-on atoms in fcc Cu and bcc W using molecular dynamics, J. Nucl. Mater. 467 (2015) 457—464.

[24] A.E. Sand, S.L. Dudarev, K. Nordlund, High energy collision cascades in tungsten: dislocation loops structure and clustering scaling laws, Europhys. Lett. 103 (2013) 46003.

[25] A.E. Sand, K. Nordlund, S.L. Dudarev, Radiation damage production in massive cascades initiated by fusion neutrons in tungsten, J. Nucl. Mater. 455 (2014) 207—211.

[26] E. Zarkadoula, D.M. Duffy, K. Nordlund, et al., Electronic effects in high-energy radiation damage in tungstens, J. Phys. Condens. Matter 27 (2015) 135401.

[27] Y. Chen, Y.H. Li, N. Gao, et al., New interatomic potentials of W, Re and W-Re alloy for radiation defects, J. Nucl. Mater. 502 (2018) 141—153.

[28] D.M. Duffy, A.M. Rutherford, Including the effects of electronic stopping and electron—ion interactions in radiation damage simulations, J. Phys. Condens. Matter 19 (2007), 016207.

[29] A.M. Rutherford, D.M. Duffy, The effect of electron—ion interactions on radiation damage simulations, J. Phys. Condens. Matter 19 (2007) 496201.

[30] S. Plimpton, Fast parallel algorithms for short-range molecular dynamics, J. Comput. Phys. 117 (1995) 1—19.

[31] J.F. Ziegler, J.P. Biersack, U. Littmark, The Stopping and Range of Ions in Matter, Pergamon, New York, 1985.

[32] F. Maury, M. Biget, P. Vajda, et al., Frenkel pair creation and stage I recovery in W crystals irradiated near threshold, Radiat. Eff. 38 (1978) 53—65.

[33] G.J. Ackland, R. Thetford, An improved N-body semi-empirical model for

[34] N. Juslin, B.D. Wirth, Interatomic potentials for simulation of He bubble formation in W, J. Nucl. Mater. 432 (2013) 61—66.

[35] M.C. Marinica, L. Ventelon, M.R. Gilbert, et al., Interatomic potentials for modelling radiation defects and dislocations in tungsten, J. Phys. Condens. Matter 25 (2013) 395502.

[36] A.E. Sand, J. Dequeker, C.S. Becquart, et al., Non-equilibrium properties of interatomic potentials in cascade simulations in tungsten, J. Nucl. Mater. 470 (2016) 119—127.

[37] Standard Practice for Neutron Radiation Damage Simulation by Charge-Particle Irradiation, E521-96, Annual Book of ASTM Standards 12.02, American Society for Testing and Materials, Philadelphia, 1996, p. 1.

[38] G.J. Martyna, M.L. Klein, M. Tuckerman, Nosé—Hoover chains: the canonical ensemble via continuous dynamics, J. Phys. Chem. 97 (1992) 2635—2643.

[39] R.E. Stoller, The role of cascade energy and temperature in primary defect formation in iron, J. Nucl. Mater. 276 (2000) 22—32.

[40] K. Nordlund, R.S. Averback, Point defect movement and annealing in collision cascades, Phys. Rev. B 56 (1997) 2421—2431.

[41] N. Juslin, V. Jansson, K. Nordlund, Simulation of cascades in tungsten—helium, Philos. Mag. A 90 (2010) 3581—3589.

[42] A. Stukowski, Visualization and analysis of atomistic simulation data with OVITO-the open visualization tool, Model. Simul. Mater. Sci. Eng. 18 (2010), 015012.

[43] A. Stukowski, V.V. Bulatov, A. Arsenlis, Automated identification and indexing of dislocations in crystal interfaces, Model. Simul. Mater. Sci. Eng. 20 (2012), 085007.

[44] M.W. Finnis, J.E. Sinclair, A simple empirical N-body potential for transition metals, Philos. Mag. A 50 (1984) 45—55.

[45] P.M. Derlet, D. Nguyen-Manh, S.L. Dudarev, Multiscale modeling of crowdion and vacancy defects in body-centered-cubic transition metals, Phys. Rev. B 76 (2007), 054107.

[46] X.W. Zhou, H.N.G. Wadley, R.A. Johnson, et al., Atomic scale structure of sputtered metal multilayers, Acta Mater. 49 (2001) 4005—4015.

[47] W. Setyawan, A.P. Selby, N. Juslin, et al., Cascade morphology transition in bcc metals, J. Phys. Condens. Matter 27 (2015) 225402.

[48] K. Vörtler, C. Björkas, D. Terentyev, et al., The effect of Cr concentration on radiation damage in Fe—Cr alloys, J. Nucl. Mater. 382 (2008) 24—30.

[49] E. Antoshchenkova, L. Luneville, D. Simeone, et al., Fragmentation of displacement cascades into subcascades: a molecular dynamics study, J. Nucl. Mater. 458 (2015) 168—175.

[50] A.I. Ryazanov, E.V. Metelkin, E.V. Semenov, Modeling of cascade and sub-cascade formation at high PKA energies in irradiated fusion structural materials, J. Nucl. Mater. 386—388 (2009) 132—134.

[51] X. Yi, A.E. Sand, D.R. Mason, et al., Direct observation of size scaling and elastic interaction between nano-scale defects in collision cascades, Europhys. Lett. 110 (2015) 36001.

[52] E. Zarkadoula, S.L. Daraszewicz, D.M. Duffy, et al., The nature of high-energy radiation damage in iron, J. Phys. Condens. Matter 25 (2013) 125402.

[53] L. Malerba, D. Terentyev, P. Olsson, et al., Molecular dynamics simulation of displacement cascades in Fe-Cr alloys, J. Nucl. Mater. 329—333 (2004) 1156—1160.

[54] D.A. Terentyev, L. Malerba, R. Chakarova, et al., Displacement cascades in Fe—Cr: a molecular dynamics study, J. Nucl. Mater. 349 (2006) 119—132.

[55] Y. Chen, J. Fang, L. Liu, et al., The interactions between rhenium and interstitial-type defects in bulk tungsten: a combined study by molecular dynamics and molecular statics simulations, J. Nucl. Mater. 522 (2019) 200—211.

[56] A.E. Sand, D.R. Mason, A.D. Backer, et al., Cascade fragmentation: deviation from power law in primary radiation damage, Mater. Res. Lett. 5 (2017) 357—363.

[57] T. Hwang, A. Hasegawa, K. Tomura, et al., Effect of neutron irradiation on rhenium cluster formation in tungsten and tungsten-rhenium alloys, J. Nucl. Mater. 507 (2018) 78—86.

[58] X. Yi, M.L. Jenkins, M. Briceno, et al., In situ study of self-ion irradiation damage in W and W—5Re at 500°C, Philos. Mag. A 93 (2013) 1715—1738.

[59] H. Xu, R.E. Stoller, Y.,N. Osetsky, et al., Solving the puzzle of interstitial loop formation in bcc Iron, Phys. Rev. Lett. 110 (2013) 265503.

[60] Q. Peng, F. Meng, Y. Yang, et al., Shockwave generates <100> dislocation loops in bcc iron, Nat. Commun. 9 (2018) 4880.

[61] N. Gao, J. Chen, R.J. Kurtz, et al., New understanding of nano-scale interstitial dislocation loops in BCC iron, J. Phys. Condens. Matter 29 (2017) 455301.

[62] A.F. Calder, D.J. Bacon, A.V. Barashev, et al., On the origin of large interstitial clusters in displacement cascades, Philos. Mag. A 90 (2010) 863—884.

[63] F. Granberg, J. Byggmästar, A.E. Sand, et al., Cascade debris overlap mechanism of <100> dislocation loop formation in Fe and FeCr, Europhys. Lett. 119 (2017) 56003.